Multi-MeV electrons observed by CRRES during solar cycle 22

R. T. Desai[1,2,3*], J. Perrin[1], N. P. Meredith[2], S. A. Glauert[2], S. Ruparelia[1], W. R. Johnston[4]

[1]Centre for Fusion, Space & Astrophysics, University of Warwick, UK

[2]British Antarctic Survey, Cambridge, UK

[3]Blackett Laboratory, Imperial College London, London, UK

Abstract

The Combined Release and Radiation Effects Satellite (CRRES) observed the response of the Van Allen radiation belts to peak solar activity within solar cycle 22. This study analyses the occurrence and loss timescales of relativistic electrons within the CRRES High Energy Electron Fluxometer (HEEF) dataset, including during several large geomagnetic storms that flooded the slot region with multi-MeV electrons and which allow the first definitive multi-MeV lifetimes to be calculated in this region. The HEEF loss timescales are otherwise broadly in agreement with those from later solar cycles but differences include longer-lasting sub-MeV electrons near the inner region of the outer belt and faster decaying multi-MeV electrons near geosynchronous orbit. These differences are associated with higher levels of geomagnetic activity, a phenomenon that enables the spread in the results to be parameterised accordingly. The timescales generally appear well-bounded by Kp-dependent theoretical predictions but the variability within the spread is however not always well-ordered by geomagnetic activity. This reveals the limits of pitch-angle diffusion in accounting for the decay of elevated electron fluxes following geomagnetic storms.

1 Introduction

The Van Allen electron radiation belts consist of two concentric tori encircling the Earth with energies extending up to several MeV [van Allen, 1959]. Satellites are designed to mitigate or avoid the impacts of these "killer" electrons which can lead to the triggering of phantom commands and component failure [e.g. Baker et al., 2013, Hands et al., 2018]. The precipitation of energetic particles also directly influences the ionisation and conductivities of the upper atmosphere, and its coupling back to the geospace environment [e.g. Roble and Rees, 1977, Orsolini et al., 2005]. The dynamics of trapped relativistic electron populations are thus a primary focus of space weather research.

The electron radiation belts typically exhibit a two-belt structure, as commonly ordered by the Roederer [1970] L* parameter. A stable so-called inner belt peaks between L* ≈ 1–2 [Selesnick et al., 2007] and a highly variable outer belt extends between L* ≈ 3–8 [Glauert et al., 2018]. This canonical picture can however rapidly change during geomagnetic storms, with additional peaks in relativistic particles fluxes, i.e. new radiation belts, forming at various distances to the Earth, including inside the slot region. The first famous example occurred on 24 March 1991, where a large interplanetary shock near-instantaneously injected a new ultra-relativistic belt extending up to over 50 MeV inside the slot region [Blake et al., 1992]. A further significant event occurred during solar cycle 23 following the Hallowe'en storms of 2003 where the outer belt reformed inside the slot region and into the inner belt as a result of enhanced convection and erosion of the plasmasphere [Baker et al., 2004]. This again occurred in solar cycle 25, when the Mother's/Gannon Day storm of May 2024 resulted in elevated fluxes forming inside the slot region [Pierrard et al., 2024]. The reordering of the outer belt into multiple distinct outer belts is also commonly

*corresponding author: ravindra.desai@warwick.ac.uk

occurring following geomagnetic storms [e.g. Pinto et al., 2018, Vampola, 1971, Baker et al., 2013, Chen et al., 2024].

Elevated electron fluxes in the inner magnetosphere, following geomagnetic storms, are observed to decay exponentially across timescales of days-weeks, a phenomenon associated with pitch-angle scattering into the atmospheric loss cone [Meredith et al., 2006, 2009, Baker et al., 2004, Claudepierre et al., 2020]. This process provides a direct method to test diffusion theory [Lyons, 1974, Kennel et al., 1985, Glauert and Horne, 2005, Albert, 2005] and its application within 3-d radiation belt models [e.g. Fok et al., 2001, Shprits et al., 2009, Su et al., 2010, Reeves et al., 2012, Glauert et al., 2014]. As a general overview the following very low frequency (VLF) waves have found to be significant. Within the slot region, the dominant modes have been found to be plasmaspheric hiss [Lyons et al., 1972, Meredith et al., 2007], lightning-generated whistlers [e.g. Lauben et al., 2001] and magnetosonic waves [Ma et al., 2016, Wong et al., 2022]. Further out, hiss continues to play an important role for electron loss in the outer radiation belt both within the plasmasphere [Summers et al., 2004, Meredith et al., 2006] and in plasmaspheric plumes [Summers et al., 2008]. In addition, electromagnetic ion cyclotron (EMIC) [Miyoshi et al., 2008, Ross et al., 2021] and whistler-mode chorus waves [Shprits et al., 2007, Wang and Shprits, 2019, Wang et al., 2024] and outward radial diffusion to the magnetopause [Shprits et al., 2006, Mann et al., 2016] may also contribute to electron loss in the outer radiation belt. Anthopogenic VLF whistlers and Coulomb collisions have also been found to be effective in the inner belt and slot region [Ripoll et al., 2014, Cunningham et al., 2018, Ross et al., 2019b].

Multi-MeV electron loss timescales have been empirically calculated within a few studies but the energy discrimination has often been limited to a single energy channel [e.g. West Jr. et al., 1981, Seki et al., 2005, Ripoll et al., 2015, Baker et al., 2007]. The Van Allen Probe electron lifetimes reported by Claudepierre et al. [2020] addressed this, determining decay rates within six differential energy channels extending from 1 – 4 MeV. This study addresses the analysis of multi-MeV electrons observed by CRRES during solar cycle 22, providing decay rates within six energy channels up to 4.55 MeV. Moreover, during the VAP mission multi-MeV electrons weren't seen inside L*=2.8 [Baker et al., 2014] whereas in this study we find that CRRES regularly observed multi-MeV electrons inside the slot region. This enables the first calculation of well-resolved lifetimes in this region. To investigate the variability of the loss timescales we also parameterise the results by geomagnetic activity to allow an activity-dependent comparison of electron loss timescales with decay rates predicted by pitch angle diffusion theory.

The paper is structured as follows. In Section 2 we outline the concept of pitch angle diffusion and the approach used to calculate the theoretical decay rates. In Section 3 we introduce the CRRES instrument and dataset and the automated algorithm used to derive the empirical loss timescales. In Section 4 we then present the lifetime analysis of multi-MeV electrons during the severe geomagnetic storms that flooded the slot region and the automated retrieval of lifetimes through the entire dataset. Section 5 then contrasts these with the theoretical solutions and previously reported loss timescales. Section 6 then summmarises the results of the study.

2 Pitch Angle Diffusion Theory

Pitch angle diffusion is caused by cyclotron and landau resonances. Under the assumption of quasi-linear theory of timescales longer than a drift-period, the pure pitch angle diffusion equation for particle flux, f, as a function of time, t, and equatorial pitch angle, α_0, can be written as

$$\frac{\partial f}{\partial t} = \frac{1}{T\sin(2\alpha_0)} \frac{\partial}{\partial \alpha_0}\bigg|_{L^*,E} \left(T\sin(2\alpha_0) D_{\alpha\alpha} \frac{\partial f}{\partial \alpha_0} \right), \tag{1}$$

where $D_{\alpha\alpha}$ represent pitch angle diffusion coefficients and $\mathrm{T}(\alpha_0) = 1.3 - 0.56\ \sin\alpha_0$ as the latitude dependence of the bounce period. The solution to this differential equation can be assumed to have the exponentially decaying function [Lyons et al., 1972],

$$f = Ae^{(-t/\tau)}, \tag{2}$$

for an equatorially mirroring pitch angle distribution $A(\alpha_0)$ and decay constant, τ. This leaves

$$\frac{d}{d\alpha_0}\left(D_{\alpha\alpha}T\sin(2\alpha_0)\frac{dA}{d\alpha_0}\right)+\frac{T\sin(2\alpha_0)}{\tau}A=0, \tag{3}$$

which can be solved as a boundary value problem [Albert, 1994, Meredith et al., 2006] for a given pitch angle distribution and as a function of chosen diffusion coefficients. The eigenvalues of the operator specify the time scales of the diffusion process [e.g. Albert and Shprits, 2009, Schulz and Lanzerotti, 1974]. The lowest order eigenvalues yield increasingly longer timescales and these appear dominant within observations reported so far at both equatorial and high latitudes [Meredith et al., 2006, Baker et al., 2007, Claudepierre et al., 2020]. However, this may not always be the case if the timescales of the diffusion process are longer than the timescales acting and the higher-order eigenvalues act across similar timescales to those examined [Albert, 1994, O'Brien et al., 2008]. The exponentially decaying solution in Equation 2, also allows empirical e-folding decays to be derived from observational data, as described in the next section, to serve as a direct comparison to these theoretical solutions.

In this study we utilise the Kp-dependent theoretical approach to Equation 3 of Glauert et al. [2024] which accounts for plasmaspheric hiss, upper/lower band chorus waves, EMIC waves, VLF transmitters, lightning-generated whistlers (LGW) and magnetosonic waves, derived within the Olson and Pfitzer [1977] field model. Glauert et al. [2024] reported loss timescales up to 1 MeV and at the single multi-MeV channel 2.6 MeV. In this study, we show lifetimes within each of the six HEEF energy channels up to 4.55 MeV. The hiss diffusion coefficients are derived from the wave model of Meredith et al. [2018] from $2\leq L*\leq 6$ using Dynamics Explorer, Double Star, Cluster, THEMIS, and VAP observations, and the PADIE code [Glauert and Horne, 2005]. The chorus diffusion coefficients are derived using the observations reported by Meredith et al. [2020] for $2\leq L*\leq 10$ based upon Dynamic Explorer, Double Star , THEMIS, and VAP, and the PADIE code. The VLF transmitter diffusion coefficients were derived by Ross et al. [2019a] for $L*<3$ using VAP observations. The EMIC diffusion coefficients were derived by Ross et al. [2021] and Ross et al. [2020] from $3.25\leq L*\leq 7$ using VAP observations. The LGW diffusion coefficients were calculated using PADIE for $2\leq L\leq 3$ based on the Green et al. [2020] VAP wave model and the densities of Ozhogin et al. [2012] from the IMAGE spacecraft. The magnetosonic diffusion coefficients are derived from Wong et al. [2022] using VAP observations. Pitch angle diffusion due to collisions with the atmosphere inside the loss cone is also incorporated as described in Selesnick [2016] for a tilted dipolar magnetic field with specified eccentricity.

3 HEEF Dataset

3.1 Instrumentation

The data used in this study is derived from the Combined Release and Radiation Effects Satellite (CRRES) High Energy Electron Fluxometer (HEEF) instrument which obtained measurements in an equatorial geostationary transfer orbit moving through radial distances of 1.05-6.26 Earth radii at an inclination of 18°, from 25 July 1990 till 12 October 1991 [Gussenhoven et al., 1996]. The HEEF instrument [Dichter et al., 1993] was designed to measure the electrons in ten channels from 1 to 10 MeV with 10 degree half-angle pitch angle spectra obtained through the spinning of the platform and the CRRES magnetometer. The instrument utilised two solid state detectors and a bismuth germinate crystal scintilator and an anti-coincidence plastic scintillator, to correlate a particle detection and determine energy and species. The HEEF instrument was extensively calibrated prior to launch [Dichter and Hanser, 1995] however, shortly after launch it became necessary to turn off a heater in the HEEF compartment with the result that HEEF operated at temperatures significantly different than planned. Since the operation of the bismuth germinate (BGO) crystal scintillator is temperature sensitive, further calibration work on HEEF was completed using on-orbit data and laboratory calibration of a flight spare unit [Hanser, 1995]. Despite this the complete unfolding and convergence of the in-flight dataset was never accomplished with potential errors highlighted within the flux values [McKellar, 1996].

In 2014, further empirical calibration factors were applied to the HEEF data to re-establish the utility of this dataset [Johnston et al., 2014]. Starting from a data set version with temperature and dead-time

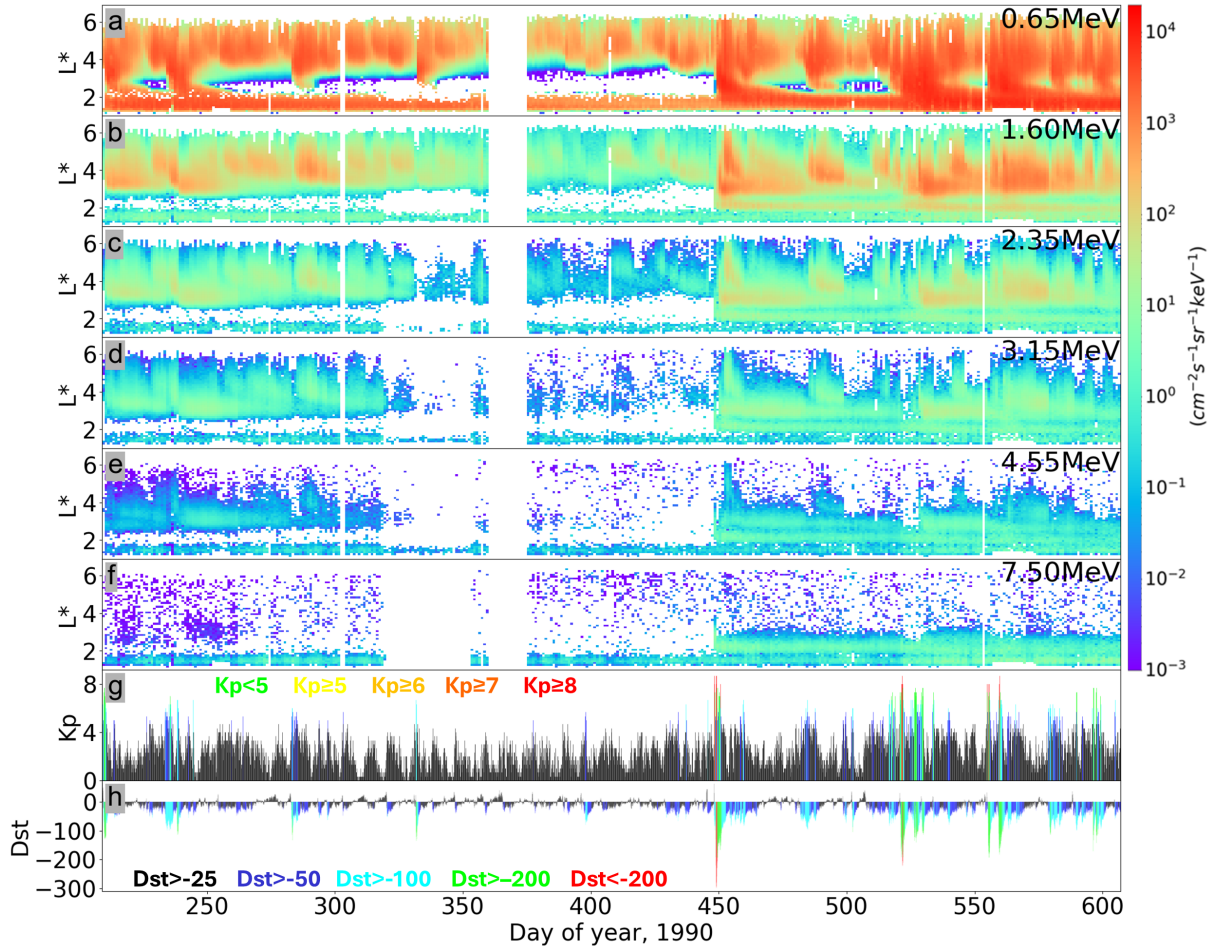

Figure 1: HEEF daily averaged differential number flux at each second energy channels outlined in Table 1 in subplots a-f throughout the CRRES mission. Subplot (g) and (h) show the respective corresponding Kp and Dst indices.

corrections applied, further corrections were implemented, including removal of data with incomplete pitch angle distributions and cross-calibration with the CRRES Medium Electron Analyser (MEA) [Vampola et al., 1992]. The resultant dataset consists of one-minute averages of differential electron fluxes separated into 5° pitch angle bins, with L* values derived from the Olson and Pfitzer [1977] magnetic field model. Table 1 outlines ten differential energy channels, eight of which are intrinsic to the instrument mode of operation and two additional differential channels (0.65 and 0.95 MeV) derived from differencing pairs of integral channels [Brautigm and Bell, 1995]. For further description of the cleaning of the data set and the contents, the reader is referred to Johnston et al. [2014].

3.2 Deriving Empirical Loss Timescales

Empirical electron lifetimes can be calculated using the same solution to Equation 1 through fitting the timescale, τ, in Equation 2 directly to the HEEF data. We use a linear fit to the natural logarithm of the data to reduce interference from the largest fluxes. The derivation of electron lifetimes utilises daily averaged electron fluxes and their temporal evolution within individual energy bins over extended periods. The decays are fitted too using the exponential function over periods of over 25 data points ($\approx$ 5 days). The data is initially smoothed prior to fitting over a 11-point window ($\approx$1 days). To determine the quality of the fits we used the Pearson correlation coefficient, a value between -1 and 1, 0 being no correlation, -1 being a perfect negative correlation and 1 a perfect positive. Following periods of exponential decay, the

Table 1: Mid-point and ranges of the HEEF energy channels used in this study [Brautigm and Bell, 1995, McKellar, 1996].

Channel	0	1	2	3	4	5	6	7	8	9	10
$\mathbf{E}_{lower}$	0.50	0.85	1.25	1.70	2.10	2.50	2.90	3.30	4.10	4.95	6.66
$\mathbf{E}_{mid}$	0.65	0.95	1.60	2.00	2.35	2.75	3.15	3.75	4.55	5.75	7.50
$\mathbf{E}_{upper}$	<0.80	<1.05	<1.70	<2.10	<2.50	<2.90	<3.30	<4.10	<4.95	<6.6	<8.55

flux levels exhibit significant variations likely representing a balance of production and loss and radial transport and the assumptions behind using Equations 2 are no longer valid.

This process is automated with predefined criteria specifying the determination of a fit to a decay timescale. This technique of identifying electron flux decays using an automated algorithm is analogous to that described in Meredith et al. [2009]. The data does not consist of daily averages, rather the average of each pass through 0.1 L^* shell ranges. The electron distribution functions, $A(\alpha_0)$, are taken between local pitch angles 60-120 degrees and ±15 degrees magnetic latitude. For automatic fitting, each flux data point is sequentially selected to be the starting point for a fit, with the initial end point determined by the given minimum fit range value. The resulting fit is used to find the Pearson coefficient and standard deviation. If a fit is found, i.e. the algorithm returns a negative Pearson coefficient with a value less than the threshold value of -0.95, the end point is incremented, with this process continuing until the Pearson value is no longer lower than the threshold. This incrementation of the fit length is continued within a given tolerance of Pearson values to avoid local minima. If the fit returns a Pearson with a value greater than the threshold, both the start and end points are incremented and the fitting process is repeated on the new data range until the Pearson value becomes less than the threshold, i.e. a new decay is found.

4 HEEF Dataset Analysis

Figure 1 shows the HEEF data throughout the CRRES mission ordered by day numbers continuous from day 1=1 Jan 1990. Specifically, we show the averaged electron differential number flux as a function of L* and time at energies of (a-f) 0.65, 1.60, 2.35, 3.15, 4.55, and 7.50 MeV. In the absence of continuous upstream solar wind measurements, panels (g) and (h), respectively, show a trace of the Kp and disturbance storm time (Dst) indices to contextualise the surrounding geomagnetic activity. The Kp indices are ordered according to the NOAA geomagnetic storm scales; Kp<5, Kp≥5 (G1), Kp≥6 (G2), Kp≥7 (G3) and Kp≥8 (G4), and the disturbance storm time (Dst) indices according to the storm definition of Loewe and Prölss [1997]; Dst>-30, Dst<-50 (weak), Dst<-100 (moderate) and Dst<–200 (severe). Great/extreme events defined by Kp=9 (G5) and Dst<-350 were not observed.

Figure 1 shows during the first half of the mission there were four strong storms and these are all associated with enhancements of 0.65 MeV electrons down to low values of L* with some events extending deep into the slot region and even the inner radiation belt. These storms tend also to be associated with flux enhancements at higher energies, up to 4.55 MeV. Interestingly, there is also a storm that doesn't quite reach the threshold to be classified as a strong storm a few days before the second strong storm and this is also associated with enhancements of 0.65 MeV electrons to low L*. In sharp contrast there were 12 strong storms and two severe storms during the second half of the mission which result in a larger number of significant enhancements of 0.65 MeV electrons down to low L* and larger flux enhancements at higher energies.

The Kp index notably shows different scalings to the Dst in that in the second half of the mission three storms reach Kp=9- (G4), an equivalence between them in contrast to the Dst index showing the single event on March 1991 reaching an intensity significantly greater than the others. The Kp index also reveals several peaks within each of the three G4 storms, for example in March 1991 showing two Kp=9- peaks corresponding to a first large compression reported early on 24 March [Blake et al., 1992] where the magnetopause was pushed inside geosychronous orbit for several hours [Elphic et al., 1991] and then a further large compression late on 24 March and 25 March, reported to drive large magnetopause oscillations near geosychronous orbit [Cahill and Winckler, 1992, Desai et al., 2021b]. The Kp index is a mid-latitude metric and this could be caused by motion of the auroral oval due to dynamic pressure

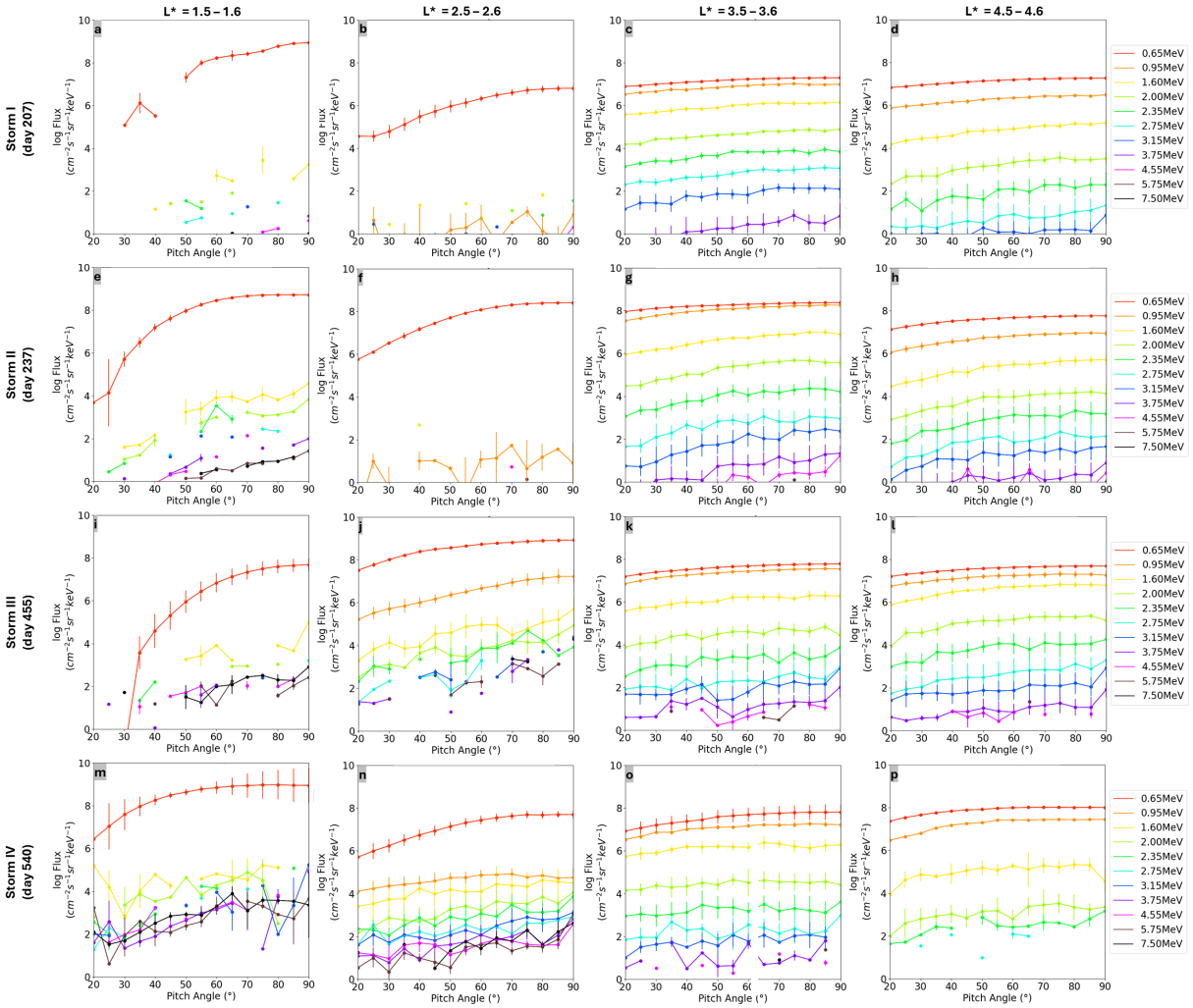

Figure 2: Pitch angle distributions at different L* shells, used as a measure of identifying coherent or contaminated electron spectra. Day 207 = 26 Jul 1990; day 237 = 25 Aug 1990; day 455 = 31 Mar 1991; day 540 = 24 Jun 1991.

enhancements associated with successive coronal mass ejections [Desai et al., 2020]. The Dst index is conversely an equatorial index, associated with southward directed interplanetary magnetic fields and build-up of the ring current, and this therefore captures the geomagnetic response across longer time-periods. Several studies have highlighted that radiation belt flux variations may be better correlated with the Kp index [Borovsky and Shprits, 2017, Wang et al., 2024], and the HEEF loss timescales and theoretical solutions in this study are parameterised as a function of the Kp index.

Figure 2 shows examples of the HEEF energy and pitch angle (PA) distributions corresponding to the data in Figure 1 during four periods of elevated fluxes and at four distinct radial distances, in the inner belt at L* = 1.5, in the heart of the slot region at L* = 2.5 and then in the outer belt at L* = 3.5 and L* = 4.5.

In Figures 1 and 2, an inner electron radiation belt is visible at L*<2 for the whole mission. In the lowest-energy channel 0, centred at 0.65 MeV, the dynamics of this inner belt correlate well with enhanced fluxes at higher L shells. The PA spectra at energy channel 0 (0.65 MeV) MeV at L* = 1.5 in Figure 2 also agrees well with expectations appearing symmetric about 90°. The next energy channel 1 (0.95 MeV) is, however, devoid of fluxes in the inner belt. The higher energy channels do display counts here, but the non-uniform spectra are suggestive that this is proton contamination at multi-MeV energies in

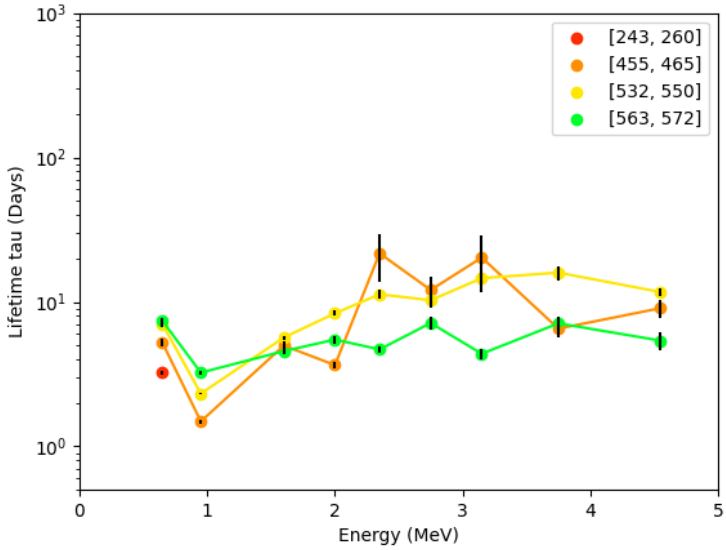

Figure 3: Slot region electron differential number flux at L*=2.5 as a function of day number for the entire CRRES mission. (a-i) shows 0.65, 0.95, 1.60, 2.00, 2.35, 2.75, 3.15, 3.75, and 4.55 MeV electrons, within a L*=0.1 bin. Fitted exponential decays are overplotted in red for a minor storm at the storm of the mission and three severe storms during the latter half.

the inner zone. We are therefore unable to ascertain whether multi-MeV electrons appeared within the inner belt during the CRRES mission.

The outer radiation belt appears highly variable throughout the CRRES mission driven by elevated geomagnetic activity. Following the geomagnetic storm of 24 March 1991, the multi-MeV electrons in the outer belt are separated into two further belts as examined by Kellerman et al. [2014] at lower energies. The corresponding energy and PA spectra are coherent up to 4.55 MeV and this multi-belt structure therefore also manifests at multi-MeV energies. The flux levels at around 10 counts appear highly variable, and we thus determine an approximate “noise floor" in the data below which we do not try to interpret signals as genuine. This effective noise floor, unfortunately, precludes the analysis in the study of the two highest energy channels 9 and 10, 5.75 and 7.5 MeV respectively, in this study.

Within the slot region, see L*= 2.5 panel in Figure 2 and Figures 1a-f, elevated flux levels start after 24 March 1991 (day 448) and extend right through to the end of the mission. The fluxes for the few orbits surrounding the injection of this new belt on day 448 [Blake et al., 1992] are not present in the dataset due to the cleaning procedures applied [Johnston et al., 2014] but the decay of this belt is visible following day 450. The corresponding energy and PA spectra in Figure 2j show coherent observations up to several MeV inside the slot region and throughout the outer belt. The further geomagnetic storms near days 525 and 560 in Figure 1 also produce elevated fluxes in the slot region of a similar or greater magnitude to those deriving from the 24 March 1991 event, with fluxes comparable to those in the outer belt. The Kp reaches similar magnitudes for these events, but the Dst index is significantly lower. These events are notable in that during solar cycle 24, multi-MeV electrons were unable to penetrate below L*=2.8 [Baker et al., 2014], with great solar activity in 2003 [Baker et al., 2004] and 2024 [Pierrard et al., 2024] required to overcome this. These also enable us to calculate slot-region loss timescales at multi-MeV energies, something that was not possible during the Van Allen probe era.

To further examine the slot-filling events, Figure 3 shows the data within an L*=0.1 bin, centred at L* = 2.5, in each energy channel up to 4.55 MeV. Most of the energy channels exhibit little data in the slot region, but three decay periods following storms in the latter part of the mission are fitted to, overlaid as red lines, with Pearson correlation coefficients all lower than –0.95, together with a decay near day 240. Figure 4 shows the resultant lifetimes as a function of energy from these periods. In the first event we only observe an electron response at 0.65 MeV, whereas in the next three events all energies are affected. The trends show increased lifetimes at sub-MeV energies which decreases to a minimum near

Figure 4: Electron loss timescales in the slot region at L* = 2.5-2.6, as a function of energy for four time-periods during the CRRES mission noted in the legend.

1 MeV associated with increased pitch angle diffusion into the loss cone [Glauert et al., 2024, see Fig 3 therein]. The lifetimes then increase again and level out at multi-MeV energies.

To examine electron lifetimes throughout the CRRES era, Figure 5 shows data in the lowest energy channel, 0.65 MeV, now ordered as a function of radial distance. The fits are once again overlaid on top of the data. The automated algorithm returns increasing numbers of fits at the intermediate L shells examined, overall visibly well-capturing exponentially decaying fluxes. A few flux decreases can however also be seen to be missed. In some instances, e.g. Figure 5c, it might appear that there are two stages to the decay process, for example in Figure 6h after day 450. These often appear as a shallow gradient followed by a greater decrease in the differential number flux. Further non-uniform decays are evident near the peak fluxes themselves over shorter time periods, with notably rounded structures at the lower L shells. This may in part be due to increasing production close to the initial event, varying geomagnetic activity levels during the decay, or potentially different eigenmodes dominating the pitch angle diffusion. At the lowest L shells, the electron fluxes decay over extended periods of tens-hundreds of days. The automated nature of the algorithm struggles with this extended period due to a short minimum fit window required to be defined to resolve the shorter timescales at larger L shells. While tweaks to the fitting procees improve these, this is difficult to scale across all L shells due to the rapid gradient in lifetimes between the inner belt and slot region and assumptions behind exponentially decaying fluxes following an enhancement. We also wish to maintain the automated neutrality of the algorithm and, despite the difficulties in the inner zone, a few fits are returned that are representative of this region. The decay periods are well-represented by the exponential fits in the region $3.0 \leq L^* \leq 4.5$. At $L^* \geq 5$, only a few fits are visible. This may again in part be due to the algorithm being difficult to optimise for such a

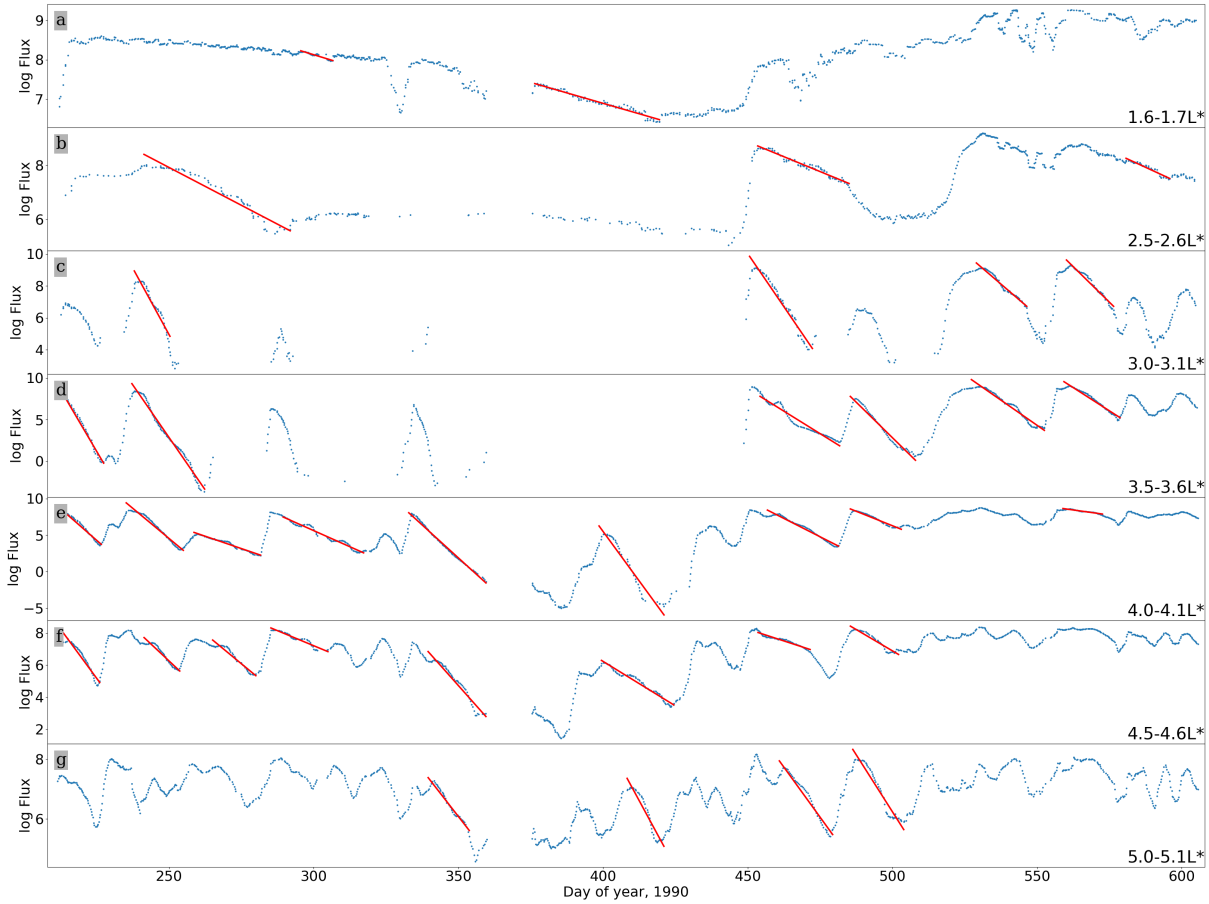

Figure 5: The 0.65 MeV electron energy number flux as a function of day number for the entire CRRES mission for (a-g) 1.6-1.7L*, 2.5-2.6L*, 3.0-3.1L*, 3.5-3.6L*, 4.0-4.1L*, 4.5-4.6L* and 5.0-5.1L*. The fitted exponential decays are overplotted in red

wide spread in lifetimes where, at these greater radial distances, further transport processes associated with radial diffusion [Su et al., 2010], drift shell splitting [Sibeck et al., 1987] and drift orbit bifurcations [Desai et al., 2021a] become significant.

Figure 6 displays the results across all L^* shells and energies with each fit colored according to its mean Kp index. The average fit at each 0.1 L^* bin is also shown as a black line together with error bars representing the standard deviation.

At the lowest L^* shells in the inner belt, the lifetimes of the 0.65 MeV electrons are tens to over a hundred days. The difficulty in fitting to these L shells, see Figure 5a and associated discussion, means the fits appear to be biased towards shorter time-periods where the two fits appear of a greater gradient than the seemingly constant decay between day 220 and 325. This appears to have been caused by storms at or prior to the start of the mission followed by relatively quiet conditions for 100 days which resulted in an even longer decay period than those shown, of ≈200 days. Given these extended timescales, these fluxes may have partially resulted from the extreme storm of March 1989 [Boteler, 2019]. These long timescales are also evident in that during the second half of the mission, where geomagnetic activity was higher, the 0.65 MeV flux is unable to decay and appears to be largely on an upward trend from around day 450 to 550. The decreased slot region lifetimes between $L^* = 2$-3 are well captured at this energy, as in Figure 3, before the lifetimes increase to another smaller maximum with increasing radial distance near $L^* = 4$.

The lifetimes of the 0.95 MeV electrons are lower than those of the 0.65 MeV electrons near $L^* = 4.0$

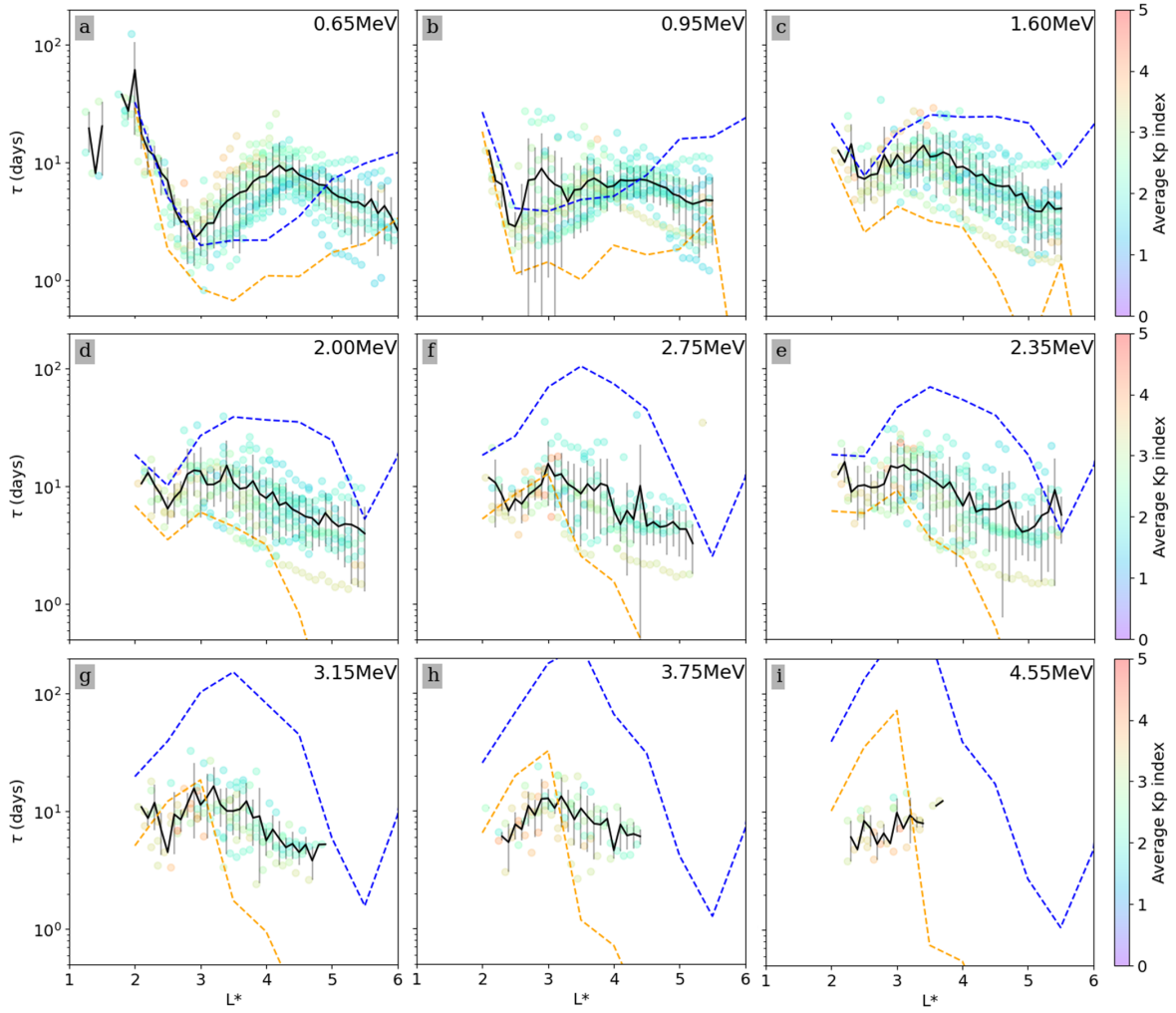

Figure 6: HEEF lifetimes of multi-MeV electrons presented for each energy bin as a function of L*. The raw data are coloured according to the average Kp index during the event, the black line shows the average fit with error bars showing the standard deviation of calculated lifetimes. Pitch angle diffusion theoretical predictions are shown at Kp = 0-1 and 4-5.

but this trend does not extend into the slot region where the reverse is true. There is a peak near L* = 2.5-3 but this is due to a large spread in the data here. At energies greater than 1 MeV, the peak lifetime in the outer belt moves inward with increasing energy from L* ≈ 4.5 at 1 MeV down to L* ≈ 3 at 4.55 MeV. The location of the shortest lifetimes in the slot region fluxes also move inwards, with increasing energies displaying longer lifetimes.

In addition to the average trends, the Kp values of each fitted lifetime provides information on how the decays scale with geomagnetic activity. At higher L* shells, i.e. greater than L* = 3, elevated geomagnetic activity appears to drive fast losses with some of the shortest timescales showing Kp values near 5. At the lower L*'s, however, and particularly at te lowest energy channel of 0.65 MeV, high Kp values often correspond to longer decay timescales. High Kp scenarios will still result in injections from the tail and acceleration of energetic particles and this trend is therefore explained by sustained production of electrons occurring alongside pitch angle scattering, a phenomenon which preferentially affects lower energies. This is further discussed in Section 5.

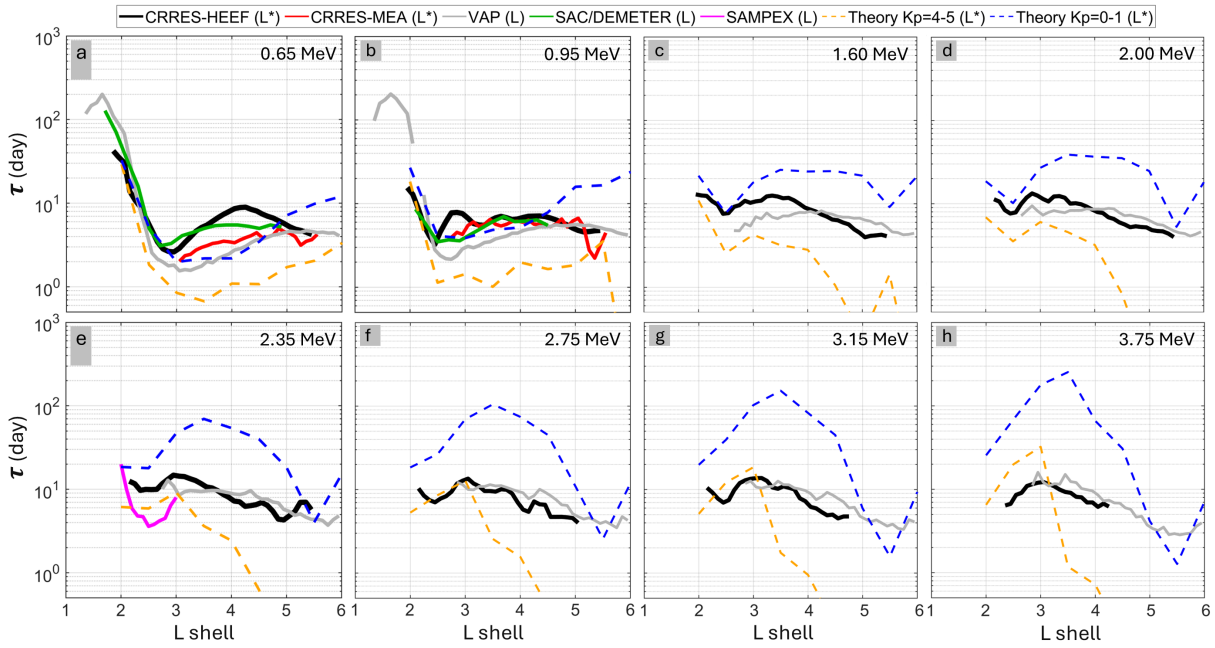

Figure 7: Experimental and theoretical electron lifetimes as a function of L shell for (a-h) 0.65, 0.95, 1.60, 2.00, 2.35, 2.75, 3.15 and 3.75 MeV electrons respectively. The black, red, grey, green and pink traces represent the experimental lifetimes derived from the CRRES-HEEF (this study), MEA [Meredith et al., 2006], VAP [Claudepierre et al., 2020], SAC/DEMETER [Benck et al., 2010] and SAMPEX datasets [Meredith et al., 2009], respectively. The dashed blue and orange traces represent the pitch angle diffusion theoretical lifetimes for quiet and high geomagnetic activity, respectively. All data is interpolated to the HEEF energies, whereas the SAMPEX 2–6 MeV data are associated with the 2.35 MeV HEEF channel.

5 Comparisons & Discussion

To compare the HEEF results with pitch angle diffusion theory, the pitch angle diffusion lifetimes described in Section 2 are also plotted in Figure 6 with dashed lines representing decays for minimum and maximum Kp levels of 0-1 and 4-5 respectively. The average HEEF results are also plotted in Figure 7 with further empirical results from other spacecraft. These include coinciding measurements from the CRRES-Medium Energy Analyser (CRRES-MEA) [Meredith et al., 2006], from VAP between 2012 and 2019 [Claudepierre et al., 2020], from ACE/DEMETER from year 2000 [Benck et al., 2010] and from SAMPEX in 2003 [Meredith et al., 2009]. All the lifetimes are interpolated to the HEEF energy channels with the 2–6 MeV SAMPEX data judged to best represent 2.35 MeV, see for example the relative fluxes in Figure 2. The CRRES and theoretical results are expressed in terms of L* whereas the further empirical results are expressed in terms of dipole L shell. The subsequent discussion utilises the term L shell when comparisons are between lifetimes utilising these different measures of the radial location of electron orbits.

In Figure 6, the pitch angle diffusion theory matches the observed trend of increased lifetimes near the inner belt at 0.65 MeV and depressed lifetimes in the slot region. In the inner part of the outer radiation belt, the quiet-time theoretical lifetimes at this energy are a factor of two or more smaller than the observed lifetimes in the region $3.2 < L* < 4.6$. These larger HEEF lifetimes are similar to those observed by SAC/DEMETER in 2001 [Benck et al., 2010] and also by ATS-1 [Vampola, 1971] see Claudepierre et al. [2020, Fig. 2f therein]. This however is not observed in the VAP lifetimes. Further examination of Figure 6 reveals a cause of this discrepancy. The underlying HEEF fits, most visibly between L* = 3-4, feature a clustering of lifetimes at the lower lifetimes ranges, similar to those reported by the MEA and closer to those observed by VAP. However, an additional clustering above

this demonstrates a bi-modality within the dataset, with this second cluster corresponding to higher Kp values. This bimodality is also identifiable in the underlying fits on Figure 5d and 5e where many of the fitted lifetimes have shallower gradients.

The consequent differences in the average lifetimes in Figure 7a may therefore have been caused by differing levels of geomagnetic activity, with CRRES having observed an average Kp index of 2.67 compared to the VAP average of 1.67. This can still be explained through three distinct mechanisms. Firstly, the intensity of geomagnetic storms were significantly greater in solar cycle 22 compared with solar cycle 24. These, during the latter half of the mission, indeed appear to be associated with the slower decays in Figure 5. These intense and longer lasting events also influence the average Kp indices of a decay and thus skew the decay rates to higher Kp values, producing a "left-right" Kp bias as indeed shown by Meredith et al. [2006, Figure 6 therein]. Secondly, disturbed geomagnetic conditions would more frequently reoccur during a decay period. This is visibly consistent with several of the decays observed, see for example the decays days 270 and 295 in Figure 5e-f where large injections/enhancements occur during the decay process. Thirdly, it is well-known that typical solar wind parameters have declined significantly over the past 50 years, with differences between the 70-90s and 2010s having been highlighted as high as tens to over fifty percent [McComas et al., 2013]. Such long-term trends in the radiation belts are difficult to study due to their inherent variability, and the inconsistency of dedicated missions, but the longitudinal comparison between CRRES and VAP data, may enable such trends to be identified. Higher ambient solar wind driving might therefore have resulted in enhanced magnetotail loading and substorms injections. In addition, each of the above three points might also cause the plasmasphere/plasmaspheric hiss to extend to lower L shells during the CRRES era than during the VAP era. Lower energies are particularly affected by this loss mechanism, as found by the evolution of the energy spectra within VAP and CRRES observations [Zhao et al., 2019, Johnston et al., 2010].

The bimodality in the decays rates is less apparent in the lifetimes beyond $L^* = 4$, with the high Kp lifetimes now more often lower than the low Kp lifetimes and the average even lower than the VAP observations beyond $L^* = 5$. The CRRES-MEA [Meredith et al., 2006] lifetimes are lower than the HEEF lifetimes in the outer belt between L = 2-4 although are higher than determined by VAP. The reason behind the differences with the MEA dataset is initially surprising given the HEEF and MEA datasets have been cross-calibrated [Johnston et al., 2014]. Comparisons between the Meredith et al. [2006] fits at the MEA energy channel of 0.604 MeV (not shown) and the HEEF energy channel of 0.65 MeV in Figure 5, indicate that the MEA algorithm is biased towards shorter fits and the HEEF fitting algorithms towards longer fits. This is evident near days 270, 495 and 520 in Figure 5e as these events feature some intrinsic variability in the fluxes, and Kp and DST indices, see Figure 1, but which overall are still well-approximated by periods of exponential decay if the algorithm is able to move past local minima in the Pearson values. This type of discrepancy may also explain further differences between the various studies reporting electron loss timescales.

A further factor to be considered is that Brautigm and Bell [1995] adopt an energy span of 0.50-0.80 MeV for HEEF energy channel 0 and the electron lifetimes derived from HEEF for 0.65 MeV are therefore influenced by longer lifetime electrons than the MEA lifetimes. This is the energy-dependent decay seen in Meredith et al. [2006] and Zhao et al. [2019], i.e. as lower energy electrons are depleted the higher energy ones will dominate and may thus influence the lifetime more.

It should be noted that Claudepierre et al. [2020] identify contamination due to Brehmstrahlung from higher energy electrons as a further potential cause of these longer lifetimes in the MEA and SAC/DEMETER datasets. As CRRES did not downlink the data required to identify and correct this effect, it is not possible to ascertain the extent to which HEEF was affected via the same method as VAP. However, we don't tend to observe features at 0.65 MeV similar to those reported by Claudepierre et al. [2020] at 0.6 MeV in the VAP uncorrected data, which tend to show two different decay periods when the contamination is present, with a rapid initial decay and then a more gradual decay. This suggests that contamination from Bremsstrahlung is not so important for the HEEF data. The 0.65 MeV lifetimes also peak beyond $L^* = 4$, whereas the multi-MeV lifetimes peak below $L^* = 3$ and so the multi-MeV electrons are not directly correlated with the elevated lifetimes at 0.65 MeV. The HEEF and VAP lifetimes at higher energies also show good agreement, see subsequent discussion, and the HEEF lifetimes are actually shorter in the outer belt, consistent with higher accompanying geomagnetic activity.

At 0.95 MeV, Figure 6b and 7b, the theory bounds many of the fitted lifetimes but is lower than the

observations when scaling by geomagnetic activity with half the fitted lifetimes outside the upper bound predicted by theory. The HEEF, MEA and SAC/DEMETER observations however show similar lifetimes at all L shells. The VAP lifetimes appear slightly lower, consistent again with the lower geomagnetic activity argument discussed previously with reference to Figure 7a. At 1.60 MeV, Figure 6c and 7c, the HEEF and VAP observations show similar average values at L shells of 4.5-5.5 but further in, the HEEF results decay more slowly in-line with the previously discussed high Kp-associated decays. This trend is similar at 2.00 MeV, but the HEEF lifetimes are noticeably shorter than the VAP lifetimes beyond L shells of 4. The HEEF lifetimes are similar to the VAP lifetimes at 2.35, 3.75 and 3.15 MeV, but again do decay slightly faster at L shells greater than 4. The HEEF observations provide the first calculation of lifetimes at >4 MeV, and comparisons with previous observations at 4.55 MeV are therefore not possible. The fact that the VAP average lifetimes peak further out than the HEEF lifetimes may also in part be due to the VAP lifetimes using L instead of L* [e.g. Roederer and Lejosne, 2018].

At energies of 1.6, 2, 2.3 and 2.75 MeV (Figure 6c-f), the theory captures the full spread in the HEEF data. At 2.75 MeV, Figure 6g, the theory still bounds the data at L shells greater than 3.5 but at lower radial distances and in the slot region diverges slightly with the prediction at Kp=4-5 appearing above many of the HEEF lifetimes. This trend is exaggerated further at 3.75 MeV and 4.55, Figure 6h-g, with the theory predicting longer lifetimes in the slot region than observed and a wide spread in possible lifetimes throughout the outer belt. At 4.55 MeV, the theory predicts even longer lifetimes than at 3.75 MeV, an increase not seen in the HEEF decay rates.

At L shells less than 4, discrepancies between theory and observations have been highlighted to potentially result from the lack of EMIC wave models [He et al., 2023] which preferentially affect larger energies, lower-frequency hiss [Ni et al., 2014] or wave-normal angle effects [Hartley et al., 2018]. The EMIC wave models used herein indeed only extend down to L* = 3.25, below which these waves are difficult to identify. The discrepancies between the observations and the theory could also well-derive from the assumption in Equation 1 of pure pitch angle diffusion. For example, Ross et al. [2021] employ 3-D modelling to better capture the decay of 2.5 MeV electrons near L = 3.5 using combined energy and radial diffusion. Su et al. [2012] indeed highlight that at L shells greater than 5, the loss timescales are largely insensitive to energy due to radial transport. It is therefore likely that radial diffusion also plays a role at lower L shells and particularly during higher levels of geomagnetic activity when the magnetopause may be more compressed.

Although the HEEF lifetimes are well-bounded by the theory, the lifetimes are not strictly ordered by geomagnetic activity, with data at lower L shells having been highlighted as corresponding to higher Kp indices. A spread in the lifetimes at higher L shells is less apparent but some of the intermediate decays associated with Kp values of 1-3 still not correctly ordering the decays. This suggests the varying role of alternative transport processes such as energy and radial diffusion.

6 Summary & Conclusions

This study has utilised the CRRES-HEEF instrment to analyse relativistic electrons during solar cycle 22 with well-resolved measurements extending from 0.65 to 4.55 MeV. The slot region was observed to be flooded with electrons up to 4.55 MeV following three intense geomagnetic storms in the latter half of the mission. Comparable events have only been observed on a few occasions since, for example during and following the Hallowe'en storm period of 2003 in solar cycle 23 [Baker et al., 2013, Meredith et al., 2009] and during the Mother's day/Gannon storm of May 2024 in solar cycle 25 [Pierrard et al., 2024], with solar cycle 24 identified as possessing an "impenetrable" barrier preventing high energy electrons from reaching below L*= 2.8 [Baker et al., 2014].

While the lack of continuous upstream solar wind observation in 1991 precludes further analysis of the upstream drivers of these slot-filling events observed by CRRES, the regularity of this phenomenon during the latter half of the mission can only be interpretted as presenting a persistent risk during large, but non-extreme, geomagnetic storms and therefore to satellites operating in slot region orbits. This directly affects constellations such as the O3B which operates at L=2.2.

The average electron loss timescales are compared to other solar cycles and several differences were highlighted. These include longer-lasting sub-MeV electrons near the inner edge of the outer belt, several

slot-filling events which allowed the first definitive timescales at multi-MeV energies to be derived, and faster decaying fluxes beyond L* $\approx$ 5. These differences are associated with higher levels of geomagnetic activity. Several reasons were put forth to explain this which included higher levels of solar and geomagnetic activity during solar cycle 22 than in subsequent cycles.

To examine the individual decay periods in more detail we also parameterise the results according to geomagnetic activity. This reveals several important trends. At higher L shells, the results are generally well-ordered by geomagnetic activity with high Kp decays often driving shorter loss timescales. Near the inner regions of the outer belt and in the slot region, however, this did not appear to be the case with a series of slow decays corresponding to high levels of activity. These persistent trends suggest that pitch angle diffusion cannot solely explain the evolution of fluxes during this periods, with other competing transport processes likely contributing.

A further outcome of this investigation is that this HEEF dataset provided valuable data regarding radiation belt dynamics during solar cycle 22, either for stand-alone investigations or boundary conditions for radiation belt modelling. Care should be taken however, particularly when interpreting absolute fluxes, with sight of the underlying energy and pitch angle spectra.

Acknowledgements

References

J. Albert and Y. Shprits. Estimates of lifetimes against pitch angle diffusion. *Journal of Atmospheric and Solar-Terrestrial Physics*, 71(16):1647–1652, 2009. ISSN 1364-6826. doi: https://doi.org/10.1016/j.jastp.2008.07.004. URL `https://www.sciencedirect.com/science/article/pii/S1364682608001818`. Toward an Integrated View of Inner Magnetosphere and Radiation Belts.

J. M. Albert. Quasi-linear pitch angle diffusion coefficients: Retaining high harmonics. *Journal of Geophysical Research: Space Physics*, 99(A12):23741–23745, 1994. doi: https://doi.org/10.1029/94JA02345. URL `https://agupubs.onlinelibrary.wiley.com/doi/abs/10.1029/94JA02345`.

J. M. Albert. Evaluation of quasi-linear diffusion coefficients for whistler mode waves in a plasma with arbitrary density ratio. *Journal of Geophysical Research (Space Physics)*, 110(A3):A03218, Mar. 2005. doi: 10.1029/2004JA010844.

D. N. Baker, S. G. Kanekal, X. Li, S. P. Monk, J. Goldstein, and J. L. Burch. An extreme distortion of the Van Allen belt arising from the 'Hallowe'en' solar storm in 2003. *Nature*, 432(7019):878–881, Dec. 2004. doi: 10.1038/nature03116.

D. N. Baker, S. G. Kanekal, R. B. Horne, N. P. Meredith, and S. A. Glauert. Low-altitude Measurements of 2-6 MeV Electron Trapping Lifetimes at 1.5 < L < 2.5. In *AGU Fall Meeting Abstracts*, volume 2007, pages SM12A–06, Dec. 2007.

D. N. Baker, S. G. Kanekal, V. C. Hoxie, M. G. Henderson, X. Li, H. E. Spence, S. R. Elkington, R. H. W. Friedel, J. Goldstein, M. K. Hudson, G. D. Reeves, R. M. Thorne, C. A. Kletzing, and S. G. Claudepierre. A Long-Lived Relativistic Electron Storage Ring Embedded in Earth's Outer Van Allen Belt. *Science*, 340(6129):186–190, Apr. 2013. doi: 10.1126/science.1233518.

D. N. Baker, A. N. Jaynes, V. C. Hoxie, R. M. Thorne, J. C. Foster, X. Li, J. F. Fennell, J. R. Wygant, S. G. Kanekal, P. J. Erickson, W. Kurth, W. Li, Q. Ma, Q. Schiller, L. Blum, D. M. Malaspina, A. Gerrard, and L. J. Lanzerotti. An impenetrable barrier to ultrarelativistic electrons in the Van Allen radiation belts. *Nature*, 515(7528):531–534, Nov. 2014. doi: 10.1038/nature13956.

S. Benck, L. Mazzino, M. Cyamukungu, J. Cabrera, and V. Pierrard. Low altitude energetic electron lifetimes after enhanced magnetic activity as deduced from sac-c and demeter data. *Annales Geophysicae*, 28(3):849–859, 2010. doi: 10.5194/angeo-28-849-2010. URL `https://angeo.copernicus.org/articles/28/849/2010/`.

J. B. Blake, W. A. Kolasinski, R. W. Fillius, and E. G. Mullen. Injection of electrons and protons with energies of tens of MeV into L < 3 on 24 March 1991. *Geophys. Res. Lett*, 19(8):821–824, Apr. 1992. doi: 10.1029/92GL00624.

J. E. Borovsky and Y. Y. Shprits. Is the dst index sufficient to define all geospace storms? *Journal of Geophysical Research: Space Physics*, 122(11):11,543–11,547, 2017. doi: https://doi.org/10.1002/2017JA024679. URL https://agupubs.onlinelibrary.wiley.com/doi/abs/10.1002/2017JA024679.

D. H. Boteler. A 21st Century View of the March 1989 Magnetic Storm. *Space Weather*, 17(10):1427–1441, Oct. 2019. doi: 10.1029/2019SW002278.

D. H. Brautigm and J. T. Bell. Crresele documentation. *Environmental Research Papers*, (1178), 1995. doi: PL-TR-95-2128. URL https://apps.dtic.mil/sti/tr/pdf/ADA301770.pdf.

J. Cahill, L. J. and J. R. Winckler. Periodic magnetopause oscillations observed with the GOES satellites on March 24, 1991. *Journ. Geophys. Res.*, 97(A6):8239–8243, June 1992. doi: 10.1029/92JA00433.

J.-L. Chen, H. Zou, Y.-X. Hao, Y.-G. Ye, Y. Miyoshi, A. Matsuoka, I. Shinohara, M. Teramoto, and S.-G. Xu. A sub-relativistic electron three-belt event in the earth's radiation belts: Observation and explanation. *Journal of Geophysical Research: Space Physics*, 129(4):e2023JA032213, 2024. doi: https://doi.org/10.1029/2023JA032213. URL https://agupubs.onlinelibrary.wiley.com/doi/abs/10.1029/2023JA032213. e2023JA032213 2023JA032213.

S. G. Claudepierre, Q. Ma, J. Bortnik, T. P. O'Brien, J. F. Fennell, and J. B. Blake. Empirically estimated electron lifetimes in the earth's radiation belts: Van allen probe observations. *Geophysical Research Letters*, 47(3):e2019GL086053, 2020. doi: https://doi.org/10.1029/2019GL086053. URL https://agupubs.onlinelibrary.wiley.com/doi/abs/10.1029/2019GL086053. e2019GL086053 10.1029/2019GL086053.

G. S. Cunningham, V. Loridan, J.-F. Ripoll, and M. Schulz. Neoclassical diffusion of radiation-belt electrons across very low l-shells. *Journal of Geophysical Research: Space Physics*, 123(4):2884–2901, 2018. doi: https://doi.org/10.1002/2017JA024931. URL https://agupubs.onlinelibrary.wiley.com/doi/abs/10.1002/2017JA024931.

R. T. Desai, H. Zhang, E. E. Davies, J. E. Stawarz, J. Mico-Gomez, and P. Iváñez-Ballesteros. Three-Dimensional Simulations of Solar Wind Preconditioning and the 23 July 2012 Interplanetary Coronal Mass Ejection. *Solar Physics*, 295(9):130, Sept. 2020. doi: 10.1007/s11207-020-01700-5.

R. T. Desai, J. P. Eastwood, R. B. Horne, H. J. Allison, O. Allanson, C. E. J. Watt, J. W. B. Eggington, S. A. Glauert, N. P. Meredith, M. O. Archer, F. A. Staples, L. Mejnertsen, J. K. Tong, and J. P. Chittenden. Drift orbit bifurcations and cross-field transport in the outer radiation belt: Global mhd and integrated test-particle simulations. *Journal of Geophysical Research: Space Physics*, 126 (10):e2021JA029802, 2021a. doi: https://doi.org/10.1029/2021JA029802. URL https://agupubs.onlinelibrary.wiley.com/doi/abs/10.1029/2021JA029802. e2021JA029802 2021JA029802.

R. T. Desai, M. P. Freeman, J. P. Eastwood, J. W. B. Eggington, M. O. Archer, Y. Y. Shprits, N. P. Meredith, F. A. Staples, I. J. Rae, H. Hietala, L. Mejnertsen, J. P. Chittenden, and R. B. Horne. Interplanetary shock-induced magnetopause motion: Comparison between theory and global magnetohydrodynamic simulations. *Geophysical Research Letters*, 48(16):e2021GL092554, 2021b. doi: https://doi.org/10.1029/2021GL092554. URL https://agupubs.onlinelibrary.wiley.com/doi/abs/10.1029/2021GL092554. e2021GL092554 2021GL092554.

B. Dichter and F. Hanser. Analyze data from crres payloads afgl-701/dosimeter and afgl- 701-4/fluxmeter. *PL-TR-92-2223, Phillips Laboratory, AFMC, Hanscom AFB, MA.*, (ADA241399):1–29, 1995. doi: D-A241399.

B. Dichter, F. Hanser, B. Sellers, and J. Hunerwadel. High energy electron fluxmeter. *IEEE Transactions on Nuclear Science*, 40(2):252–255, 1993. doi: 10.1109/23.212350.

R. C. Elphic, M. F. Thomsen, D. J. M. K. R. Moore, and S. J. Bame. Geosynchronous Observations of the Magnetopause and Related Phenomena on March 24 and 25, 1991. *AGU Fall Meeting December 9-13, 1991*, 8(9-10):319, Dec. 1991. doi: SH11A-50935(1).

M.-C. Fok, T. E. Moore, and W. N. Spjeldvik. Rapid enhancement of radiation belt electron fluxes due to substorm dipolarization of the geomagnetic field. *JGR*, 106(A3):3873–3882, Mar. 2001. doi: 10.1029/2000JA000150.

S. A. Glauert and R. B. Horne. Calculation of pitch angle and energy diffusion coefficients with the PADIE code. *Journal of Geophysical Research (Space Physics)*, 110(A4):A04206, Apr. 2005. doi: 10.1029/2004JA010851.

S. A. Glauert, R. B. Horne, and N. P. Meredith. Three-dimensional electron radiation belt simulations using the BAS Radiation Belt Model with new diffusion models for chorus, plasmaspheric hiss, and lightning-generated whistlers. *Journal of Geophysical Research (Space Physics)*, 119(1):268–289, Jan. 2014. doi: 10.1002/2013JA019281.

S. A. Glauert, R. B. Horne, and N. P. Meredith. A 30-year simulation of the outer electron radiation belt. *Space Weather*, 16(10):1498–1522, 2018. doi: https://doi.org/10.1029/2018SW001981. URL `https://agupubs.onlinelibrary.wiley.com/doi/abs/10.1029/2018SW001981`.

S. A. Glauert, J. W. Atkinson, J. P. Ross, and R. B. Horne. A New Model of Electron Pitch Angle Distributions and Loss Timescales in the Earth's Radiation Belts. *Journal of Geophysical Research (Space Physics)*, 129(6):e2023JA032249, June 2024. doi: 10.1029/2023JA032249.

A. Green, W. Li, Q. Ma, X.-C. Shen, J. Bortnik, and G. B. Hospodarsky. Properties of lightning generated whistlers based on van allen probes observations and their global effects on radiation belt electron loss. *Geophysical Research Letters*, 47(17):e2020GL089584, 2020. doi: https://doi.org/10.1029/2020GL089584. URL `https://agupubs.onlinelibrary.wiley.com/doi/abs/10.1029/2020GL089584`. e2020GL089584 2020GL089584.

M. Gussenhoven, E. Mullen, and D. Brautigam. Improved understanding of the earth's radiation belts from the crres satellite. *IEEE Transactions on Nuclear Science*, 43(2):353–368, 1996. doi: 10.1109/23.490755.

A. D. P. Hands, K. A. Ryden, N. P. Meredith, S. A. Glauert, and R. B. Horne. Radiation effects on satellites during extreme space weather events. *Space Weather*, 16(9):1216–1226, 2018. doi: https://doi.org/10.1029/2018SW001913. URL `https://agupubs.onlinelibrary.wiley.com/doi/abs/10.1029/2018SW001913`.

F. Hanser. Data analysis procedures for the crres payloads afgl-701-2/dosimeter and agrl-701-4/fluxmeter and application of the data analysis results to improve the static and dynamic models of the earth's radiation belts. *PL-TR-92-2223, Phillips Laboratory, AFMC, Hanscom AFB, MA.*, (PL-TR-95-2103), 1995.

D. P. Hartley, C. A. Kletzing, O. Santolík, L. Chen, and R. B. Horne. Statistical properties of plasmaspheric hiss from van allen probes observations. *Journal of Geophysical Research: Space Physics*, 123(4):2605–2619, 2018. doi: https://doi.org/10.1002/2017JA024593. URL `https://agupubs.onlinelibrary.wiley.com/doi/abs/10.1002/2017JA024593`.

Z. He, J. Xu, C. Wang, L. Dai, B. Ni, and I. Roth. Evidence of h+-band emic waves in the inner radiation belt observed by van allen probes during magnetic storms. *Journal of Geophysical Research: Space Physics*, 128(3):e2022JA031088, 2023. doi: https://doi.org/10.1029/2022JA031088. URL `https://agupubs.onlinelibrary.wiley.com/doi/abs/10.1029/2022JA031088`. e2022JA031088 2022JA031088.

W. R. Johnston, C. D. Lindstrom, and G. P. Ginet. Characterization of radiation belt electron energy spectra from CRRES observations. In *AGU Fall Meeting Abstracts*, volume 2010, pages SM33C–1925, Dec. 2010.

W. R. Johnston, C. D. Lindstrom, and G. P. Ginet. Crres medium electron sensor a (mea) and high energy electron fluxmeter (heef): Cross-calibrated data set description. *Air Force Research Laboratory Space Vehicles Directorate 3550 Aberdeen Avenue SE Kirtland AFB, NM 87117-5776*, 2014. doi: AFRL-RV-PS-TR-2014-0016. URL `https://apps.dtic.mil/sti/pdfs/ADA604519.pdf`.

A. C. Kellerman, Y. Y. Shprits, D. Kondrashov, D. Subbotin, R. A. Makarevich, E. Donovan, and T. Nagai. Three-dimensional data assimilation and reanalysis of radiation belt electrons: Observations of a four-zone structure using five spacecraft and the verb code. *Journal of Geophysical Research: Space Physics*, 119(11):8764–8783, 2014. doi: https://doi.org/10.1002/2014JA020171. URL `https://agupubs.onlinelibrary.wiley.com/doi/abs/10.1002/2014JA020171`.

C. F. Kennel, J. P. Edmiston, and T. Hada. A quarter century of collisionless shock research. *Washington DC American Geophysical Union Geophysical Monograph Series*, 34:1–36, Jan. 1985. doi: 10.1029/GM034p0001.

D. S. Lauben, U. S. Inan, and T. F. Bell. Precipitation of radiation belt electrons induced by obliquely propagating lightning-generated whistlers. *Journal of Geophysical Research: Space Physics*, 106 (A12):29745–29770, 2001. doi: https://doi.org/10.1029/1999JA000155. URL `https://agupubs.onlinelibrary.wiley.com/doi/abs/10.1029/1999JA000155`.

C. A. Loewe and G. W. Prölss. Classification and mean behavior of magnetic storms. *Journal of Geophysical Research: Space Physics*, 102(A7):14209–14213, 1997. doi: https://doi.org/10.1029/96JA04020. URL `https://agupubs.onlinelibrary.wiley.com/doi/abs/10.1029/96JA04020`.

L. R. Lyons. General relations for resonant particle diffusion in pitch angle and energy. *Journal of Plasma Physics*, 12(1):45–49, Aug. 1974. doi: 10.1017/S0022377800024910.

L. R. Lyons, R. M. Thorne, and C. F. Kennel. Pitch-angle diffusion of radiation belt electrons within the plasmasphere. *JGR*, 77(19):3455, Jan. 1972. doi: 10.1029/JA077i019p03455.

Q. Ma, W. Li, R. M. Thorne, J. Bortnik, C. A. Kletzing, W. S. Kurth, and G. B. Hospodarsky. Electron scattering by magnetosonic waves in the inner magnetosphere. *Journal of Geophysical Research: Space Physics*, 121(1):274–285, 2016. doi: https://doi.org/10.1002/2015JA021992. URL `https://agupubs.onlinelibrary.wiley.com/doi/abs/10.1002/2015JA021992`.

I. R. Mann, L. G. Ozeke, K. R. Murphy, S. G. Claudepierre, D. L. Turner, D. N. Baker, I. J. Rae, A. Kale, D. K. Milling, A. J. Boyd, H. E. Spence, G. D. Reeves, H. J. Singer, S. Dimitrakoudis, I. A. Daglis, and F. Honary. Explaining the dynamics of the ultra-relativistic third Van Allen radiation belt. *Nature Physics*, 12(10):978–983, Oct. 2016. doi: 10.1038/nphys3799.

D. J. McComas, N. Angold, H. A. Elliott, G. Livadiotis, N. A. Schwadron, R. M. Skoug, and C. W. Smith. Weakest Solar Wind of the Space Age and the Current "Mini" Solar Maximum. *ApJ*, 779(1):2, Dec. 2013. doi: 10.1088/0004-637X/779/1/2.

B. McKellar. UNFOLDING THE HIGH ENERGY ELECTRON FLUX FROM CRRES FLUXMETER MEASUREMENTS. *Air Force Institute of Technology Air University*, PhD Thesis, July 1996. doi: AFIT/GAP7ENP796D-8.

N. P. Meredith, R. B. Horne, S. A. Glauert, R. M. Thorne, D. Summers, J. M. Albert, and R. R. Anderson. Energetic outer zone electron loss timescales during low geomagnetic activity. *Journal of Geophysical Research (Space Physics)*, 111(A5):A05212, May 2006. doi: 10.1029/2005JA011516.

N. P. Meredith, R. B. Horne, S. A. Glauert, and R. R. Anderson. Slot region electron loss timescales due to plasmaspheric hiss and lightning-generated whistlers. *Journal of Geophysical Research: Space Physics*, 112(A8), 2007. doi: https://doi.org/10.1029/2007JA012413. URL `https://agupubs.onlinelibrary.wiley.com/doi/abs/10.1029/2007JA012413`.

N. P. Meredith, R. B. Horne, S. A. Glauert, D. N. Baker, S. G. Kanekal, and J. M. Albert. Relativistic electron loss timescales in the slot region. *Journal of Geophysical Research (Space Physics)*, 114(A3): A03222, Mar. 2009. doi: 10.1029/2008JA013889.

N. P. Meredith, R. B. Horne, T. Kersten, W. Li, J. Bortnik, A. Sicard, and K. H. Yearby. Global model of plasmaspheric hiss from multiple satellite observations. *Journal of Geophysical Research: Space Physics*, 123(6):4526–4541, 2018. doi: https://doi.org/10.1029/2018JA025226. URL https://agupubs.onlinelibrary.wiley.com/doi/abs/10.1029/2018JA025226.

N. P. Meredith, R. B. Horne, X.-C. Shen, W. Li, and J. Bortnik. Global model of whistler mode chorus in the near-equatorial region (18). *Geophysical Research Letters*, 47(11):e2020GL087311, 2020. doi: https://doi.org/10.1029/2020GL087311. URL https://agupubs.onlinelibrary.wiley.com/doi/abs/10.1029/2020GL087311. e2020GL087311 10.1029/2020GL087311.

Y. Miyoshi, K. Sakaguchi, K. Shiokawa, D. Evans, J. Albert, M. Connors, and V. Jordanova. Precipitation of radiation belt electrons by emic waves, observed from ground and space. *Geophysical Research Letters*, 35(23), 2008. doi: https://doi.org/10.1029/2008GL035727. URL https://agupubs.onlinelibrary.wiley.com/doi/abs/10.1029/2008GL035727.

B. Ni, W. Li, R. M. Thorne, J. Bortnik, Q. Ma, L. Chen, C. A. Kletzing, W. S. Kurth, G. B. Hospodarsky, G. D. Reeves, H. E. Spence, J. Bernard Blake, J. F. Fennell, and S. G. Claudepierre. Resonant scattering of energetic electrons by unusual low-frequency hiss. *Geophysical Research Letters*, 41(6):1854–1861, 2014. doi: https://doi.org/10.1002/2014GL059389. URL https://agupubs.onlinelibrary.wiley.com/doi/abs/10.1002/2014GL059389.

T. P. O'Brien, M. D. Looper, and J. B. Blake. Eigenmode analysis of pitch-angle diffusion of energetic electrons in the outer zone. *Journal of Geophysical Research: Space Physics*, 113(A8), 2008. doi: 10.1029/2007JA012679. URL https://agupubs.onlinelibrary.wiley.com/doi/abs/10.1029/2007JA012679.

W. P. Olson and K. A. Pfitzer. Magnetospheric magnetic field modeling. annual scientific report. Technical report, McDonnell Douglas Astronautics Co., Huntington Beach, CA (USA), 01 1977. URL https://www.osti.gov/biblio/7212748.

Y. J. Orsolini, G. L. Manney, M. L. Santee, and C. E. Randall. An upper stratospheric layer of enhanced hno3 following exceptional solar storms. *Geophysical Research Letters*, 32(12), 2005. doi: https://doi.org/10.1029/2004GL021588. URL https://agupubs.onlinelibrary.wiley.com/doi/abs/10.1029/2004GL021588.

P. Ozhogin, J. Tu, P. Song, and B. W. Reinisch. Field-aligned distribution of the plasmaspheric electron density: An empirical model derived from the image rpi measurements. *Journal of Geophysical Research: Space Physics*, 117(A6), 2012. doi: https://doi.org/10.1029/2011JA017330. URL https://agupubs.onlinelibrary.wiley.com/doi/abs/10.1029/2011JA017330.

V. Pierrard, A. Winant, E. Botek, and M. Péters de Bonhome. The Mother's Day Solar Storm of 11 May 2024 and Its Effect on Earth's Radiation Belts. *Universe*, 10(10):391, Oct. 2024. doi: 10.3390/universe10100391.

V. A. Pinto, J. Bortnik, P. S. Moya, L. R. Lyons, D. G. Sibeck, S. G. Kanekal, H. E. Spence, and D. N. Baker. Characteristics, occurrence, and decay rates of remnant belts associated with three-belt events in the earth's radiation belts. *Geophysical Research Letters*, 45(22):12,099–12,107, 2018. doi: https://doi.org/10.1029/2018GL080274. URL https://agupubs.onlinelibrary.wiley.com/doi/abs/10.1029/2018GL080274.

G. D. Reeves, Y. Chen, G. S. Cunningham, R. W. H. Friedel, M. G. Henderson, V. K. Jordanova, J. Koller, S. K. Morley, M. F. Thomsen, and S. Zaharia. Dynamic Radiation Environment Assimilation Model: DREAM. *Space Weather*, 10(3):03006, Mar. 2012. doi: 10.1029/2011SW000729.

J. F. Ripoll, J. M. Albert, and G. S. Cunningham. Electron lifetimes from narrowband wave-particle interactions within the plasmasphere. *Journal of Geophysical Research (Space Physics)*, 119(11):8858–8880, Nov. 2014. doi: 10.1002/2014JA020217.

J.-F. Ripoll, Y. Chen, J. F. Fennell, and R. H. W. Friedel. On long decays of electrons in the vicinity of the slot region observed by heo3. *Journal of Geophysical Research: Space Physics*, 120(1):460–478, 2015. doi: https://doi.org/10.1002/2014JA020449. URL https://agupubs.onlinelibrary.wiley.com/doi/abs/10.1002/2014JA020449.

R. G. Roble and M. H. Rees. Time-dependent studies of the aurora: Effects of particle precipitation on the dynamic morphology of ionospheric and atmospheric properties. *PSS*, 25(11):991–1010, Nov. 1977. doi: 10.1016/0032-0633(77)90146-5.

J. G. Roederer. *Dynamics of geomagnetically trapped radiation.* , 1970.

J. G. Roederer and S. Lejosne. Coordinates for Representing Radiation Belt Particle Flux. *Journal of Geophysical Research (Space Physics)*, 123(2):1381–1387, Feb. 2018. doi: 10.1002/2017JA025053.

J. P. J. Ross, N. P. Meredith, S. A. Glauert, R. B. Horne, and M. A. Clilverd. Effects of vlf transmitter waves on the inner belt and slot region. *Journal of Geophysical Research: Space Physics*, 124(7):5260–5277, 2019a. doi: https://doi.org/10.1029/2019JA026716. URL https://agupubs.onlinelibrary.wiley.com/doi/abs/10.1029/2019JA026716.

J. P. J. Ross, N. P. Meredith, S. A. Glauert, R. B. Horne, and M. A. Clilverd. Effects of vlf transmitter waves on the inner belt and slot region. *Journal of Geophysical Research: Space Physics*, 124(7):5260–5277, 2019b. doi: https://doi.org/10.1029/2019JA026716. URL https://agupubs.onlinelibrary.wiley.com/doi/abs/10.1029/2019JA026716.

J. P. J. Ross, S. A. Glauert, R. B. Horne, C. E. Watt, N. P. Meredith, and E. E. Woodfield. A new approach to constructing models of electron diffusion by emic waves in the radiation belts. *Geophysical Research Letters*, 47(20):e2020GL088976, 2020. doi: https://doi.org/10.1029/2020GL088976. URL https://agupubs.onlinelibrary.wiley.com/doi/abs/10.1029/2020GL088976. e2020GL088976 10.1029/2020GL088976.

J. P. J. Ross, S. A. Glauert, R. B. Horne, C. E. J. Watt, and N. P. Meredith. On the Variability of EMIC Waves and the Consequences for the Relativistic Electron Radiation Belt Population. *Journal of Geophysical Research (Space Physics)*, 126(12):e29754, Dec. 2021. doi: 10.1029/2021JA029754.

M. Schulz and L. J. Lanzerotti. *Particle Diffusion in the Radiation Belts*, volume 7 of *Physics and Chemistry in Space*. Springer-Verlag, New York, 1974. doi: 10.1007/978-3-642-65675-0.

K. Seki, Y. Miyoshi, D. Summers, and N. P. Meredith. Comparative study of outer-zone relativistic electrons observed by akebono and crres. *Journal of Geophysical Research: Space Physics*, 110(A2), 2005. doi: https://doi.org/10.1029/2004JA010655. URL https://agupubs.onlinelibrary.wiley.com/doi/abs/10.1029/2004JA010655.

R. S. Selesnick. Stochastic simulation of inner radiation belt electron decay by atmospheric scattering. *Journal of Geophysical Research: Space Physics*, 121(2):1249–1262, 2016. doi: https://doi.org/10.1002/2015JA022180. URL https://agupubs.onlinelibrary.wiley.com/doi/abs/10.1002/2015JA022180.

R. S. Selesnick, M. D. Looper, and R. A. Mewaldt. A theoretical model of the inner proton radiation belt. *Space Weather*, 5(4), 2007. doi: https://doi.org/10.1029/2006SW000275. URL https://agupubs.onlinelibrary.wiley.com/doi/abs/10.1029/2006SW000275.

Y. Y. Shprits, R. M. Thorne, R. Friedel, G. D. Reeves, J. Fennell, D. N. Baker, and S. G. Kanekal. Outward radial diffusion driven by losses at magnetopause. *Journal of Geophysical Research: Space Physics*, 111(A11), 2006. doi: https://doi.org/10.1029/2006JA011657. URL https://agupubs.onlinelibrary.wiley.com/doi/abs/10.1029/2006JA011657.

Y. Y. Shprits, N. P. Meredith, and R. M. Thorne. Parameterization of radiation belt electron loss timescales due to interactions with chorus waves. *Geophysical Research Letters*, 34(11), 2007. doi: https://doi.org/10.1029/2006GL029050. URL https://agupubs.onlinelibrary.wiley.com/doi/abs/10.1029/2006GL029050.

Y. Y. Shprits, D. Subbotin, and B. Ni. Evolution of electron fluxes in the outer radiation belt computed with the VERB code. *Journal of Geophysical Research (Space Physics)*, 114(A11):A11209, Nov. 2009. doi: 10.1029/2008JA013784.

D. G. Sibeck, R. W. McEntire, A. T. Y. Lui, R. E. Lopez, and S. M. Krimigis. Magnetic field drift shell splitting: Cause of unusual dayside particle pitch angle distributions during storms and substorms. *Journal of Geophysical Research: Space Physics*, 92(A12):13485–13497, 1987. doi: https://doi.org/10.1029/JA092iA12p13485. URL https://agupubs.onlinelibrary.wiley.com/doi/abs/10.1029/JA092iA12p13485.

Y.-J. Su, W. R. Johnston, J. M. Albert, G. P. Ginet, M. J. Starks, and C. J. Roth. Scatha measurements of electron decay times at $5 < l < 8$. *Journal of Geophysical Research: Space Physics*, 117(A8), 2012. doi: https://doi.org/10.1029/2012JA017685. URL https://agupubs.onlinelibrary.wiley.com/doi/abs/10.1029/2012JA017685.

Z. Su, F. Xiao, H. Zheng, and S. Wang. STEERB: A three-dimensional code for storm-time evolution of electron radiation belt. *Journal of Geophysical Research (Space Physics)*, 115(A9):A09208, Sept. 2010. doi: 10.1029/2009JA015210.

D. Summers, C. Ma, and T. Mukai. Competition between acceleration and loss mechanisms of relativistic electrons during geomagnetic storms. *Journal of Geophysical Research (Space Physics)*, 109(A4):A04221, Apr. 2004. doi: 10.1029/2004JA010437.

D. Summers, B. Ni, N. P. Meredith, R. B. Horne, R. M. Thorne, M. B. Moldwin, and R. R. Anderson. Electron scattering by whistler-mode ELF hiss in plasmaspheric plumes. *Journal of Geophysical Research (Space Physics)*, 113(A4):A04219, Apr. 2008. doi: 10.1029/2007JA012678.

A. L. Vampola. Natural variations in the geomagnetically trapped electron population. *In E. A. Warman (Ed.), Proceedings of the National Symposium on Natural and Manmade Radiation in Space*, Aerospace Corp., El Segundo, Calif.):539–547, Aug. 1971. doi: 72N17671.

A. L. Vampola, J. V. Osborn, and B. M. Johnson. CRRES magnetic electron spectrometer AFGL-701-5A (MEA). *Journal of Spacecraft and Rockets*, 29(4):592–595, Aug. 1992. doi: 10.2514/3.25504.

J. A. van Allen. The Geomagnetically Trapped Corpuscular Radiation. *JGR*, 64(11):1683–1689, Nov. 1959. doi: 10.1029/JZ064i011p01683.

D. Wang and Y. Y. Shprits. On how high-latitude chorus waves tip the balance between acceleration and loss of relativistic electrons. *Geophysical Research Letters*, 46(14):7945–7954, 2019. doi: https://doi.org/10.1029/2019GL082681. URL https://agupubs.onlinelibrary.wiley.com/doi/abs/10.1029/2019GL082681.

D. Wang, Y. Y. Shprits, B. Haas, and A. Y. Drozdov. Improved lifetime model of energetic electrons due to their interactions with chorus waves. *Geophysical Research Letters*, 51(19):e2023GL107991, 2024. doi: https://doi.org/10.1029/2023GL107991. URL https://agupubs.onlinelibrary.wiley.com/doi/abs/10.1029/2023GL107991. e2023GL107991 2023GL107991.

H. I. West Jr., R. M. Buck, and G. T. Davidson. The dynamics of energetic electrons in the earth's outer radiation belt during 1968 as observed by the lawrence livermore national laboratory's spectrometer on ogo 5. *Journal of Geophysical Research: Space Physics*, 86(A4):2111–2142, 1981. doi: https://doi.org/10.1029/JA086iA04p02111. URL https://agupubs.onlinelibrary.wiley.com/doi/abs/10.1029/JA086iA04p02111.

J.-M. Wong, N. P. Meredith, R. B. Horne, S. A. Glauert, and J. P. J. Ross. Electron diffusion by magnetosonic waves in the earth's radiation belts. *Journal of Geophysical Research: Space Physics*, 127(4):e2021JA030196, 2022. doi: https://doi.org/10.1029/2021JA030196. URL `https://agupubs.onlinelibrary.wiley.com/doi/abs/10.1029/2021JA030196`. e2021JA030196 2021JA030196.

H. Zhao, W. R. Johnston, D. N. Baker, X. Li, B. Ni, A. N. Jaynes, S. G. Kanekal, J. B. Blake, S. G. Claudepierre, G. D. Reeves, and A. J. Boyd. Characterization and evolution of radiation belt electron energy spectra based on the van allen probes measurements. *Journal of Geophysical Research: Space Physics*, 124(6):4217–4232, 2019. doi: https://doi.org/10.1029/2019JA026697. URL `https://agupubs.onlinelibrary.wiley.com/doi/abs/10.1029/2019JA026697`.